PCCP

Optical deformation potential and self-trapped excitons in 2D hybrid perovskites

SCHOLARONE™
Manuscripts

Journal Name

ARTICLE TYPE

Optical deformation potential and self-trapped excitons in 2D hybrid perovskites†

Zhi-Gang Yu*

Self-trapped excitons (STEs) in two-dimensional (2D) hybrid organic-inorganic perovskites (HOIPs) emit broadband white light, suggesting a great potential of 2D HOIPs in low-cost lighting and display applications. A prerequisite for understanding STEs' properties is a correct identification of the underlying interaction that leads to the STEs. Here we show that the long-range polar coupling between electrons and optical phonons is quenched in 2D HOIPs' tightly bound excitons and cannot effect STEs. Rather, the STEs are induced by a short-range optical deformation potential (ODP) arising from phonon-modulated Pb-X quantum-well thickness. Interaction between transition dipoles in adjacent PbX_6 (X= Br or I) octahedra gives rise to highly anisotropic intra- and inter-layer exciton bandwidths. In flat (001) 2D HOIPs, both the ODP and the exciton bandwidths are susceptible to out-of-plane PbX_6 tilting but not in-plane one, and their interplay can quantitatively account for the observed temperature and structure dependences of luminescence associated with STEs. In corrugated (011) 2D HOIPs, the exciton bandwidth is further reduced and the resultant STEs have a stronger lattice distortion and broader luminescence spectrum. Our results reveal the mechanism of STE formation and suggest ways of tuning STEs and associated broadband luminescence in 2D HOIPs.

1 Introduction

Hybrid organic-inorganic perovskites (HOIPs) like $CH_3NH_3PbI_3$, with an unprecedented photovoltaic efficiency exceeding 20% from solution-processed samples, represent a revolutionary breakthrough in low-cost solar cells[1–3]. When $CH_3NH_3^+$ is replaced by a long organic ion like $C_{10}H_{21}NH_3^+$, the three-dimensional (3D) HOIP is sliced into two-dimensional (2D) layers[4]. Depending on the organic ligands' arrangement, the 2D sheets are either flat when slicing the 3D HOIPs along the (001) surface, or corrugated when slicing along the (011) surface[5]. The quasi 2D HOIPs, which can be viewed as perfect quantum-well (QW) superlattices of alternating organic and inorganic layers without interfacial roughness[4], have shown a great promise in optoelectronic applications. Solar cells based on 2D HOIPs have attained high photovoltaic efficiency[6] with a much improved environmental stability and photostability under operating conditions[7,8]. The weakened Coulomb screenings in 2D transforms loosely bound Wannier excitons in 3D HOIPs into highly confined Frenkel-like excitons with a large binding energy, as demonstrated both experimentally and theoretically[9,10]. The strong exciton binding in 2D HOIPs results in exceptional light-emitting performance[11], which can be further improved by reducing the electron-phonon coupling[12]. Acoustic and optical phonon scattering, particularly those via deformation potentials, are found to influence transport of free excitons in 2D HOIPs[13].

Compared to their 3D counterpart, 2D HOIPs[7,8,14–20] have another distinct feature: easy formation of self-trapped excitons (STEs). The concept of self-trapping can be traced to Landau[21], who showed that under a strong electron-phonon interaction, an otherwise free and delocalized electron can be trapped by the lattice, forming an immobile and highly localized low-energy state. Self-trapped particles, which can be electrons, holes, and excitons[22,23], are qualitatively different from the free ones and cannot be achieved from the latter by treating the electron-phonon coupling perturbatively (via phonon scattering). In 2D HOIPs, STEs give rise to broadband white luminescence[7,14,15,19,20]. This outstanding property, together with the increased material stability[7,8], promises a bright future of 2D HOIPs in optoelectronic applications such as display and single-component light-emitting devices, stimulating extensive studies of the STEs[19,20,24,25]. One particularly intriguing observation is that an out-of-plane PbX_6 (X is halogen element Br or I) octahedral tilt strongly facilitates the formation of STEs whereas an in-plane one does not[19]. Another puzzling observation is that corrugated 2D HOIPs tend to exhibit broader luminescence than flat ones[25]. To understand these sur-

ISP/Applied Sciences Laboratory, Washington State University, Spokane, Washington 99210, USA; Department of Physics and Astronomy, Washington State University, Pullman, Washington 99164, USA; E-mail: zhi-gang.yu@wsu.edu

prising and useful properties of STEs, one must first identify the underlying interaction that leads to STEs in 2D HOIPs.

The ionic character of HOIPs suggests a significant long-range polar coupling, H_p, between electrons and electric polarization generated by longitudinal optical (LO) phonons, especially those associated with Pb-X stretching. The matrix elements of H_p between electronic states are $\langle k|H_p|k-q\rangle = iV_p^e(q)(b_q + b_{-q}^\dagger)$, where $b_q^\dagger$ creates an LO phonon with wavevector q, k and $k \pm q$ are electron wavevectors, and coupling $V_p^e(q) \sim 1/|q|$ [26,27]. The polar coupling is the primary source of carrier scattering for temperatures $T > 100$ K in 3D $CH_3NH_3PbI_3$ [27] and responsible for formation of large [27,28] or small [29] electron and hole polarons. It has been tacitly assumed in literature that it would be responsible for STEs in 2D HOIPs as well. Close examination (see below), however, indicates that the polar coupling to the oppositely charged electron and hole is essentially canceled out in tightly bound excitons of 2D HOIPs. Hence the long-range polar coupling cannot effect STEs.

Here we show that the microscopic driving force of STEs is a deformation potential engendered by X-Pb-X stretching that modulates the thickness of individual 2D layers. This thickness modulation simultaneously increases or decreases the quantized electron and hole energies in the Pb-X QW, leading to strong exciton-phonon coupling. Using this optical deformation potential (ODP) and optical selection rules associated with excitons [30], we construct a microscopic model to describe STEs in 2D HOIPs. The observed STE properties are consistently unraveled by the interplay of the ODP and anisotropic exciton bandwidths, which can be systematically tailored via PbX_6 octahedral tilting, layer corrugation, and layer-thickness variation.

2 Exciton-phonon interactions

2.1 Phonons and electron-phonon interactions

Phonon calculations in 2D HOIPs based on first principles have been reported in literature [31]. Vibrational modes that strongly couple to conduction- and valence-band electrons in 2D HOIPs are confined in Pb-X inorganic network and have similar frequencies as in their 3D counterpart [32]. Among them are the Pb-X bending and stretching modes, which give optical branches in phonon spectra. The bending modes have an energy of $\hbar\Omega_b = 3-6$ meV and the stretching modes $\hbar\Omega_s = 11-16$ meV for bromides and iodides [31,32]. Because of the ionic character in Pb and X, these modes usually generate a dynamic longitudinal electric field along the ions' motion direction, which then interacts with charged electrons and holes, giving rise to a long-range polar coupling between electrons (holes) and LO phonons. In HOIPs, the Pb-X stretching mode has a much stronger polar coupling than the bending one [27]. In addition to optical phonons, acoustic phonons, or equivalently, elastic waves, are always present in HOIPs. Elastic waves introduce strain, ∇u, with u being the lattice distortion, and interact with electrons via a strain-induced deformation potential $E_{c(v)}\nabla u$ with $E_{c(v)}$ being the deformation-potential strength associated with the conduction (valence) band. In HOIPs and many compound semiconductors, the polar coupling is the dominant electron-phonon coupling that limits carrier transport. Only

at low temperatures with few LO phonons present, does the deformation potential between electrons and low-energy acoustic phonons manifest itself in carrier mobility [27]. It has been implicitly assumed in literature that the polar coupling is responsible for the formation of STEs in 2D HOIPs. Here we show that the polar coupling to excitons in 2D HOIPs becomes ineffective.

2.2 Quench of polar coupling to excitons

A quasi 2D HOIP, as illustrated in Fig. 1a, consists of alternating inorganic Pb-X layers with thickness of l_a and organic layers with thickness of l_b. Their corresponding dielectric constants are ε_a and ε_b with $\varepsilon_a > \varepsilon_b$. The ineffectiveness of polar coupling, H_p, to excitons in 2D HOIPs is clearly seen from the hydrogenic model of excitons. The hydrogenic model, while oversimplified as compared to more elaborated works for 2D HOIPs [10], accentuates the essence of polar coupling to a tightly bound exciton. In this model, the size and binding energy of the lowest exciton are $a_0 = \hbar^2\varepsilon/e^2\mu$ and $Z^* = \mu e^4/2\varepsilon^2\hbar^2$, with μ being the reduced mass of electron-hole pair, $\mu^{-1} = m_e^{-1} + m_h^{-1}$, m_e (m_h) the effective electron (hole) mass, and $\varepsilon \equiv (l_a\varepsilon_a + l_b\varepsilon_b)/(l_a + l_b)$ the volume-averaged dielectric constant [33]. For a typical value of $\mu = 0.15m$ (m is the free-electron mass) in 2D HOIPs [17], the large binding energy $Z^* \geq 200$ meV [4] indicates that the size of exciton $a_0 < 10$ Å [$a_0 \simeq 5$ Å and $Z^* = 470$ meV in $(C_4H_9NH_3)_2PbI_4$ [10]] is comparable to the size of PbX_6 octahedra, about 6 Å. The wavefunction for such an exciton with center-of-mass wavevector k is [34]

$$|\Phi_k\rangle = \frac{1}{\sqrt{\mathcal{V}}}e^{ik\cdot R}\frac{1}{\pi a_0^3}e^{-r/a_0}, \tag{1}$$

where $R = (m_e r_e + m_h r_h)/m_{ex}$ is the center-of-mass coordinates, $m_{ex} = m_e + m_h$, r_e (r_h) is the electron (hole) location, $r \equiv r_e - r_h$ is the relative coordinates, and $\mathcal{V}$ is the volume. The polar coupling of such an exciton is $\langle \Phi_k|H_p|\Phi_{k-q}\rangle = iV_p^{ex}(q)(b_q + b_{-q}^\dagger)$ with (see the Supplementary Information) [34]

$$\begin{aligned} V_p^{ex}(q) &= \left(\frac{4\pi\alpha_e}{\mathcal{V}}\right)^{1/2}\left(\frac{\hbar}{2m_e\Omega_s}\right)^{1/4}\frac{\hbar\Omega_s}{q}\left(\frac{1}{[1+(p_e a_0 q/2)^2]^2}\right. \\ &\quad \left. - \frac{1}{[1+(p_h a_0 q/2)^2]^2}\right), \end{aligned} \tag{2}$$

where α_e is the dimensionless polar-coupling strength of Pb-X stretching for electron [26] and $p_{e(h)} = m_{h(e)}/m_{ex}$. This coupling, as plotted in Fig. 1b, reduces to zero for long-wave phonons (small q) and reaches maximum around $q \sim 1/a_0$. For an exciton with $m_e = m_h$, contributions from oppositely charged electron and hole would exactly cancel out. The similar values of m_e and m_h together with the small a_0 in 2D HOIPs make $V_p^{ex}(q)$ weak over the entire range of q. It should be noted that for disparate electron and hole masses, as illustrated by the magenta line in Fig. 1b, the polar coupling remains sizable even if the exciton is highly confined, and is indeed the driving force of STEs in 3D alkali halides [35].
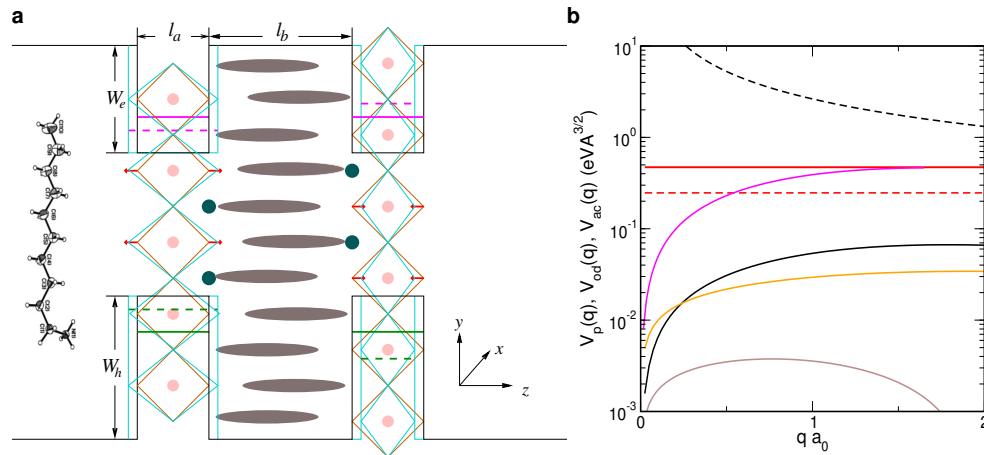
Fig. 1 ODP and polar coupling of excitons in quasi 2D HOIPs. (a) Schematic diagram illustrating the ODP. (b) Polar coupling and ODP of excitons in 2D HOIPs as a function of qa_0. In (a), alternating inorganic and organic layers form wells and walls of QWs. Cyan and brown diamonds represent PbX$_6$ inorganic octahedra with and without phonon-induced QW dilation or compression, which is described by red arrows. Shaded ovals represent organic ligands with NH$_3$ groups depicted by dark green circles. The displayed molecular structure is for a representative organic ligand, C$_{10}$H$_{21}$NH$_3$. The phonon-modulated width of QWs shifts the quantized electron (magenta lines) and hole (green lines) levels from their equilibrium values (solid lines). In (b), solid black and red lines describe the polar coupling and the ODP of an exciton with $m_e = 0.291m$ and $m_h = 0.321m$ while dashed black and red line describe those of a conduction electron with $m_e = 0.291m$. The magenta line describes the ODP of an exciton for disparate electron and hole effective masses, $m_e = 0.291m$ and $m_h = m$. Orange and brown lines describe acoustic-phonon coupling of an exciton with phonons polarized along and across the Pb-X layers (see the Supplementary Information for details). Other parameters are $\hbar\Omega_s = 14$ meV, $\alpha_e = 1.1$, $l_a = 6$ Å, and $\varepsilon = 3$.

2.3 Optical deformation potential

With polar coupling to excitons in 2D HOIPs quenched, STEs must be driven by an alternative coupling between excitons and phonons. Since the lattice distortion of STEs in 2D HOIPs is essentially confined to a single PbX$_6$ octahedron, this coupling is likely to arise from optical phonons. We notice that inorganic Pb-X layers in 2D HOIPs, as shown in Fig. 1a, can be described by perfect QWs[4] with their thickness l_a determined by the distance between the two apical X atoms in a PbX$_6$ octahedron. In such a QW, the electron motion in the inter-layer direction (z-axis) is confined, resulting in quantized energies for both conduction electrons and valence holes. For an electron (hole), the lowest energy level is $E_{e(h)} = \pi^2\hbar^2/(2m_{e(h)}l_a^2) - W_{e(h)}$ with $W_{e(h)}$ being the depth of QWs for the electron (hole). Consider the three-atom X-Pb-X chain in a PbX$_6$ octahedron normal to the Pb-X layer. Of the three eigen modes of the X-Pb-X chain, one has the central Pb stationary and the two X atoms moving out-of-phase, i.e., the B_{1g} mode[32]. The frequency of this mode (see the Supplementary Information) is determined by the spring constant of the Pb-X bond stretching and the mass of X atom and is set $\hbar\Omega_s = 14$ meV[36] throughout the paper. While stretching (contracting) of X-Pb-X in this mode does not induce an electric field because of the symmetry (homopolar)[13,37,38], it swells (reduces) the QW thickness, which decreases (increases) the quantized electron and hole energies[38] to $E_{e(h)} = \pi^2\hbar^2/[2m_{e(h)}(l_a + \delta z)^2] - W_{e(h)}$ with $\delta z/2$ being the stretching amplitude of the B_{1g} mode. For an exciton, whose energy can be expressed as $E_{ex}^0 = E_e + E_h - Z^*$, the changes in electron and hole energies influence E_{ex}^0, leading to a coupling between excitons and the X-Pb-X vibration. Since this coupling is caused by an optical-phonon-induced deformation in the Pb-X QW, it is referred to as optical deformation potential (ODP). The ODP to an exciton is strong because contributions from the electron and the hole reinforce each other. This is in stark contrast with the polar coupling in Eq. (2), where contributions from the electron and the hole negate each other. For a change in the QW thickness, δz, along the z-axis, the ODP can be expressed as $H_{od} = A\delta z$ with the coupling strength

$$A = \frac{\partial E_{ex}^0}{\partial z} \equiv \frac{\partial(E_e + E_h - Z^*)}{\partial z} = -\frac{\pi\hbar^2}{l_a^3}\left(\frac{1}{m_e} + \frac{1}{m_h}\right) + Z^*\frac{\varepsilon_a - \varepsilon_b}{\varepsilon(l_a + l_b)}. \tag{3}$$

Here in evaluating $\partial Z^*/\partial z$, which arises from the variation of ε in the presence of fluctuations in QW thickness l_a, we keep the lattice constant along the z-axis, $c \equiv l_a + l_b$, a constant. In 2D HOIPs, $\partial Z^*/\partial z$ is usually much smaller than $\partial(E_e + E_h)/\partial z$ (See the Supplementary Information).

The matrix element of ODP between free exciton states is $\langle\Phi_k|H_{od}|\Phi_{k-q}\rangle = V_{od}^{ex}(q)(b_q + b_{-q}^\dagger)$, where $V_{od}^{ex}(q) = A(\hbar/2MN\Omega)^{1/2}$, M is the mass of X ion, and N the number density of PbX$_6$ octahedra. From Fig. 1b, we see that $V_{od}^{ex}(q)$ is orders-of-magnitude stronger than $V_p^{ex}(q)$ of Eq. (2). We have also considered coupling between acoustic phonons and tightly bound excitons in 2D HOIPs (See the Supplementary Information). Acoustic phonons do not change the QW thickness which controls the quantized electron and hole energies, but rather, interact with excitons by modifying distances between adjacent PbX$_6$ octahedra. The calculated coupling between acoustic phonons and excitons, as plotted in Fig. 1b, is orders-of-magnitude weaker than the ODP and can thus be neglected in studying STEs. We emphasize that the ODP described here is unique in 2D systems and distinct from the deformation potential caused by acoustic phonons in that the former is proportional to lattice distortion, while the latter to strain.

3 STEs and their signatures in luminescence

3.1 Exciton band structure

In 2D HOIPs both free excitons (FEs) and STEs can exist, as manifested in sharp and broad peaks in luminescent spectra. If we temporarily neglect the ODP, all excitons would be FEs, i.e., electron-hole pairs bound by the Coulomb interaction. FEs are delocalized Bloch waves, whose energies with different center-of-mass wavevectors $\boldsymbol{k}$ form a band. Since in 2D HOIPs excitons have a size comparable to that of a PbX_6 octahedron, they can be regarded as Frenkel excitons in individual PbX_6 octahedra, with the band structure conveniently described by a real-space Hamiltonian,

$$H_{ex} = \sum_i E_0 c_i^\dagger c_i + \sum_{\langle ij \rangle} t_{ij} c_i^\dagger c_j. \tag{4}$$

Here $c_i^\dagger$ creates an exciton centered at the PbX_6 octahedron of site i, $|\tilde{\Phi}_i\rangle$, with energy $E_0 = E_g - Z^*$, where E_g is the energy gap between conduction and valence bands. The neighboring coupling t_{ij}, which facilitates exciton motion (hopping) from site j to an adjacent site i (denoted by $\langle ij \rangle$), originates from the interaction between transition dipoles associated with excitons, $t_{ij} = \frac{1}{|\boldsymbol{R}_{ij}|^5}[(\boldsymbol{d}_i \cdot \boldsymbol{d}_j^*)^2 |\boldsymbol{R}_{ij}|^2 - 3(\boldsymbol{d}_i \cdot \boldsymbol{R}_{ij})(\boldsymbol{d}_j^* \cdot \boldsymbol{R}_{ij})]$ [39], where $\boldsymbol{R}_i$ is the coordinate of site i, $\boldsymbol{R}_{ij} = \boldsymbol{R}_i - \boldsymbol{R}_j$, and $\boldsymbol{d}_i$ is the transition dipole moment from the ground state $|G\rangle$ to $|\tilde{\Phi}_i\rangle$, $\boldsymbol{d}_i = \langle \tilde{\Phi}_i | e\boldsymbol{r} | G \rangle$. If we approximate the lattice structure of a 2D HOIP as simple tetragonal, with intra- and inter-layer lattice constants being a and c, the Hamiltonian (4) can be diagonalized in the momentum space, $H_{ex} = \sum_{\boldsymbol{k}} E_{\boldsymbol{k}}^0 c_{\boldsymbol{k}}^\dagger c_{\boldsymbol{k}}$, where $c_{\boldsymbol{k}}^\dagger$ creates a FE with wave vector $\boldsymbol{k}$, $|\Phi_{\boldsymbol{k}}\rangle = N^{-1/2} \sum_i e^{i\boldsymbol{k} \cdot \boldsymbol{R}_i} |\tilde{\Phi}_i\rangle$, with exciton dispersion

$$E_{\boldsymbol{k}}^0 = \frac{B_\perp}{4}[2 - \cos(k_x a) - \cos(k_y a)] + \frac{1}{2}B_z[1 + \cos(k_z c)]. \tag{5}$$

Here the smallest $E_{\boldsymbol{k}}^0$ is set zero and $B_\perp$ and B_z are the intra- and inter-layer bandwidths, which characterize the kinetic energies of exciton's motion within and across Pb-X layers.

The bandwidths $B_\perp$ and B_z are proportional to t_{ij} between neighboring dipoles $\boldsymbol{d}_i$, whose magnitude and orientation are controlled by the exciton's optical selection rules. In HOIPs the conduction and valence bands have angular momenta $j_c = j_v = 1/2$, resulting in four kinds of excitons [30], where Γ_1 is dark, Γ_2 is linearly polarized along the z-axis, and doublet $\Gamma_5^\pm$ are circularly polarized in the x-y plane. Using the effective-mass model [18,30], we can express $\boldsymbol{d}_i$ in terms of intra- and inter-layer oscillator strengths $f_\perp$ and f_z, $\langle \Gamma_5^\pm | e\boldsymbol{r} | G \rangle = d_0 \boldsymbol{e}_\pm$ and $\langle \Gamma_2 | e\boldsymbol{r} | G \rangle = d_0\sqrt{f_z/f_\perp}\boldsymbol{e}_z$ with $d_0 = e\hbar\sqrt{f_\perp/(2mE_g)}$, where $\boldsymbol{e}_\pm = \mp(\boldsymbol{e}_x \pm i\boldsymbol{e}_y)/\sqrt{2}$ with $\boldsymbol{e}_q$ ($q = x, y, z$) being the unit vector along the q-axis. In 2D HOIPs, $f_\perp \gg f_z$, for example, $f_\perp = 0.7$ and $f_z = 0.01$ in $(C_{10}H_{21}NH_3)_2PbI_4$ [40], and $\boldsymbol{d}_i$ is due virtually to $\Gamma_5^\pm$. For a left-circularly polarized excitation, $\boldsymbol{d}_i = d_0 \boldsymbol{e}_+$, the intra- and inter-layer bandwidths are

$$B_\perp = \frac{2e^2\hbar^2 f_\perp}{mE_g a^3}, \ B_z = \frac{2e^2\hbar^2 f_\perp}{mE_g c^3} = B_\perp \frac{a^3}{c^3}, \tag{6}$$

are highly anisotropic in 2D HOIPs because $c \gg a$.

3.2 Formation of STEs

When the ODP of an exciton is turned on, the exciton eigenstate $|\psi\rangle$ and its energy E_{ex} satisfy the Schrödingier equation

$$[H_{ex} + H_{od}(\{Q_i\})]|\psi\rangle = E_{ex}(\{Q_i\})|\psi\rangle, \tag{7}$$

where Q_i is a dimensionless lattice distortion at site i, $Q_i \equiv (\hbar/M\Omega_s)^{-1/2}(\delta z)_i$. We have adopted the adiabatic approximation and neglected in Eq. (7) the lattice's kinetic energy. This is reasonable as we are concerned with the ground state of an STE, whose wave function is essentially determined by the potential arising from lattice distortion. Non-adiabatic effect becomes important and should be taken into account in transitions between an STE and an FE or between different STEs. Equation (7) is a self-consistent equation of lattice and exciton because the ODP, $H_{od}(\{Q_i\}) = -\gamma\sum_i Q_i |\psi(\boldsymbol{R}_i)|^2 \equiv A\sum_i (\delta z)_i |\psi(\boldsymbol{R}_i)|^2$, depends on the exciton wave function $\psi(\boldsymbol{R}_i)$ to be solved. The energy, E_{ex}, of an STE, a localized exciton state induced by the ODP, can be efficiently obtained from the poles of the T-matrix associated with the scattering potential H_{od} [39,41],

$$\det[I\delta_{ij} + \sum_l G^0(\boldsymbol{R}_{il}; E_{ex})\gamma Q_l |\psi(\boldsymbol{R}_{lj})|^2] = 0, \tag{8}$$

where $G^0(\boldsymbol{R}, E)$ is the Green's function of FEs, $G^0(\boldsymbol{R}; E) = N^{-1}\sum_{\boldsymbol{k}} e^{i\boldsymbol{k} \cdot \boldsymbol{R}}/(E - E_{\boldsymbol{k}}^0)$. We have applied this method, which is particularly effective for a short-range scattering potential, to excitons in organics [42] and to native point defects in strained layer superlattices [43]. For tightly bound excitons in 2D HOIPs, whose size is comparable to that of PbX_6 octahedra, it is reasonable to assume that STEs are localized within a unit cell. With the potential $H_{od}(\{Q_i\}) = -\gamma Q\delta_{i0}$, Eq. (8) reduces to a simple self-consistent equation of lattice distortion Q and localized exciton energy $E_{ex}(Q) < 0$ [41],

$$Q^{-1} = -\gamma G^0(0; E_{ex}). \tag{9}$$

For the anisotropic exciton dispersion in Eq. (5), we evaluate the Green's function,

$$
\begin{aligned}
G^0(0; E) = & -\frac{4}{\pi^2}\int_0^{\pi/2c} dk_z \bigg\{ \frac{1}{B_\perp + B_z[1 - \cos(k_z c)] - 2E} \\
& \times K\left(\frac{B_\perp}{B_\perp + B_z[1 - \cos(k_z c)] - 2E}\right) \\
& + \frac{1}{B_\perp + B_z[1 + \cos(k_z c)] - 2E} \\
& \times K\left(\frac{B_\perp}{B_\perp + B_z[1 + \cos(k_z c)] - 2E}\right) \bigg\},
\end{aligned}
$$

where $K(x)$ is the complete elliptic integral of the first kind. Using Eq. (9) we obtain for a given lattice distortion Q, the excitonic energy, $E_{ex}(Q)$, and the total energy $U(Q) = \frac{1}{2}\hbar\Omega Q^2 + E_{ex}(Q)$, which contains also the elastic energy due to the lattice distortion. As illustrated in Fig. 2a, potential energy surfaces (PESs) $U(Q)$ generally have three extrema: a minimum at $Q = 0$ corresponding to the FE, a minimum at $Q = Q_S$ corresponding to the STE, and a maximum at $Q = Q_B$ corresponding to the energy barrier that

separates the FE from the STE. The energies at these extrema are $U(0) = 0$, $U(Q_B) = E_B$, and $U(Q_S) = E_S$. When $E_S < 0$, the STE has a lower energy than the FE.

Figures 2b and 2c plot the calculated PES $U(Q)$ for $B_z = B_\perp$ and $B_z = 10^{-2}B_\perp$, which mimic 3D and 2D structures. We see that when the ODP is too weak, a localized state with $E_{ex} < 0$ does not exist, for to form STEs, the potential due to the ODP must be deep enough to overwhelm the kinetic energy associated with the exciton bandwidth. As the ODP strength increases, localized states with $E_{ex} < 0$ emerge, but $U(Q_S)$ may still be positive, i.e., the STE has a higher energy than the FE. In this case excitons are unlikely to populate around Q_S because photoexcited FEs do not have enough energy to reach STEs. A further increase of the ODP strength pushes $U(Q_S)$ negative and it becomes energetically possible for FEs at $Q = 0$ to move to Q_S, forming STEs. The energy barrier between the FE and the STE ensures that they both are stable and can luminesce. The dependence of $-E_S$ and E_B on the ODP strength γ are shown in Figs. 2d and 2e for $B_z = B_\perp$ and $B_z = 10^{-2}B_\perp$, respectively. Comparing the 3D and 2D structures, we see that in 2D structures the onset of STEs with $E_S < 0$ occurs at a smaller ODP strength, and for a given ODP strength, the STE energy gain $-E_S$ is larger and the barrier height E_B is smaller than in 3D structures. Figures 2f and 2g display the increase of $-E_S$ and decrease of E_B with bandwidth anisotropy $B_\perp/B_z$, respectively. When the ODP is not too strong, STEs can be present when $B_\perp/B_z$ is large but absent when $B_\perp/B_z$ is small. Thus, the confluence of strong ODP and large anisotropy in exciton bandwidths results in prevalent STEs in 2D HOIPs. Conversely, the small bandwidth anisotropy and weak ODP in 3D HOIPs suggest that STEs are difficult to form there.

3.3 Luminescence of STEs and FEs

Experimentally, FEs and STEs manifest themselves with narrow and broad peaks in photoluminescence. The integrated intensities of broad and narrow luminescence, denoted I_B and I_N, are related to the FE and STE densities, n_F and n_S, via $I_B/I_N = k'_t n_S/k_r n_F \propto n_S/n_F$, where the radiative recombination rate of STE (FE), k'_r (k_r), is insensitive to temperature. According to Ref. [19], the dynamics n_F and n_S can be expressed as

$$\frac{dn_F}{dt} = g - (k_t + k_r)n_F + k'_t n_S, \tag{10}$$

$$\frac{dn_S}{dt} = -(k'_t + k'_r + k'_{nr})n_S + k_t n_F. \tag{11}$$

Here g is generation rate of FEs, k_t (k'_t) is the transfer rate from FEs (STEs) to STEs (FEs), and k'_{nr} is the nonradiative recombination rate of STEs. Since k_t involves overcoming an energy barrier E_B, $k_t = k_t^0 e^{-E_B/k_B T}$, where k_t^0 is independent of temperature and k_B is the Boltzmann constant. Detailed balance of transfers between FEs and STEs requires $k_t/k'_t = e^{-E_S/k_B T}$. In the steady state, $dn_F/dt = dn_S/dt = 0$, and we obtain from Eqs. (10) and (11) $n_F = g(k'_t + k'_r + k'_{nr})/Z$ and $n_S = gk_t/Z$ with $Z = k_t(k'_r + k'_{nr}) + k_r(k'_t + k'_r + k'_{nr})$.

Figure 3b plots n_S and n_F as a function of reciprocal temperature. At low temperatures, n_S (n_F) increases (decreases) with T,

which is reversed at high temperatures, where n_S (n_F) decreases (increases) with T. Temperature dependence of n_S/n_F is shown in Fig. 3c. These temperature dependences can be readily understood from $n_S/n_F = k_t/(k'_t + k'_r + k'_{nr})$. At low temperatures, both k'_r and k'_{nr} are negligible, and consequently $n_S/n_F \simeq k_t/k'_r = (k_t^0/k'_r)e^{-E_B/k_B T}$. At high temperatures, k'_t can dominate over k'_r and k'_{nr}, and $n_S/n_F \simeq k_t/k'_t = e^{-E_S/k_B T}$ [20], i.e., FEs and STEs are in equilibrium. Hence from the measured temperature dependence of I_B/I_N in the low- and high-temperature regimes, one can extract E_S and E_B. For example, the temperature dependence of I_B/I_N of (HIS)PbBr$_4$ reported in Ref. [20] can be quantitatively explained by $E_S = -50$ meV and $E_B = 7$ meV, as shown in Fig. 3d.

The luminescence spectrum from STEs and FEs can be calculated from the obtained $U(Q)$ by using the Franck-Condon principle,

$$I(\omega) \propto \int_0^{Q_B} dQ e^{-(U(Q)-\mu_F)/k_B T} \delta\left(U(Q) - U_G(Q) - \hbar\omega\right)$$
$$+ \int_{Q_B}^{\infty} dQ e^{-(U(Q)-\mu_S)/k_B T} \delta\left(U(Q) - U_G(Q) - \hbar\omega\right), \tag{12}$$

where $\hbar\omega$ is the photon energy and $U_G(Q)$ is the PES of the ground state. For generality, we regard the STE and the FE as two species with respective chemical potentials μ_S and μ_F. At high temperatures when FEs and STEs are in equilibrium, $\mu_F - \mu_S = 0$; whereas at low temperatures, $\mu_F - \mu_S$ can be fixed by $n_F/n_S = (k_t^0/k'_r)e^{E_B/k_B T}$. The calculated luminescence, as delineated in Figs. 3e and 3f, contains a broad low-energy peak due to the STEs and narrow high-energy peak due to the FEs. The width of the broad peak, Δ, can be estimated by the thermal distribution of lattice distortion around Q_S of STEs, $[Q_S - \delta Q, Q_S - \delta Q]$, with $\delta Q = k_B T/2\hbar\Omega$. Consequently, $\Delta = (\partial U_G/\partial Q_S)(k_B T/\hbar\Omega)$. The broad Δ, which increases with T, is due to the large $\partial U_G/\partial Q_S$, as shown in Figs. 3e and 3f. On the other hand, luminescence from FEs is narrow because at $Q = 0$, $\partial U_G/\partial Q = \partial U/\partial Q = 0$. At low temperatures, the significant luminescence from FEs is due to the large n_F, which is not in thermal equilibrium with n_S.

4 Structural effects on STEs

4.1 Effects of PbX$_6$ Tilting

Besides the interesting temperature dependence, I_B/I_N in 2D HOIPs exhibits a strong correlation with an out-of-plane tilt of PbX$_6$ octahedra but not an in-plane one. This puzzle, which has implications in tuning STE properties, can be naturally explained by the tilting effects on the exciton bandwidths and the ODP strength. As we have shown, the transition dipole in 2D HOIPs is $d_i = d_0 e_+$, which can be represented by spherical harmonics $Y_{1+}(e_z)$. After a tilt of PbX$_6$ octahedron, the symmetry axis changes from e_z to e'_z at spherical polar angles (θ, ϕ), and the corresponding transition dipole d'_i can be obtained from the finite rotation matrix, $D^{(1)}_{m'm}(\phi, \theta, 0)$ with its three arguments being the Euler angles, $Y_{1m}(\theta, \phi) = \sum_{m'm} D^{(1)}_{m'm}(\phi, \theta, 0) Y_{1m'}(e_z)$ [33], yielding

$$d'_i(\theta, \phi) = d_0\left(\frac{1+\cos\theta}{2}e^{i\phi}e_+ + \frac{1-\cos\theta}{2}e^{-i\phi}e_- + \frac{1}{\sqrt{2}}\sin\theta e_z\right). \tag{13}$$
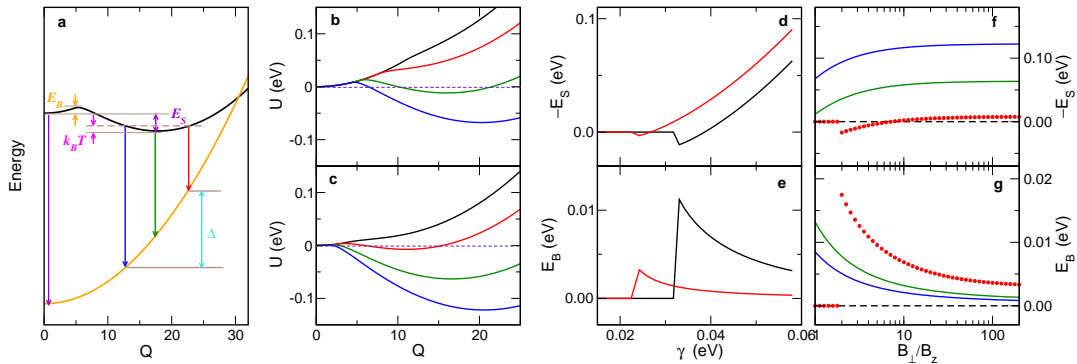
Fig. 2 PES of STEs. (a) Schematic diagram showing $U(Q)$ (black) of the exciton and $U_G(Q)$ (orange) of the ground state. (b, c) plot the calculated $U(Q)$ for $B_z = B_\perp$ and $B_z = 10^{-2}B_\perp$ for different ODP strength γ. (d, e) describe STE energy gain $-E_S$ and barrier height E_B as a function of γ. (f, g) describe $-E_S$ and E_B as a function of $B_\perp/B_z$. In (a), an energy barrier of E_B separates FEs located around $Q = 0$ from STEs. The purple arrow depicts emission from FEs. Red, green, and blue arrows represent emission from STEs with a broadband wavelengths and Δ is the width of STE luminescence. In (b), (c), (f) and (g), black, red, green, and blue lines correspond to $\gamma = 0.029$, 0.041, 0.058, and 0.071 eV. In (d) and (e), black and red lines correspond to $B_z = B_\perp$ and $B_z = 10^{-2}B_\perp$. In (b) and (c), dashed lines are $U = 0$ to guide the eye. In (d–f), $E_S = E_B = 0$ indicates no STEs are formed. $B_\perp$ is fixed at 0.12 eV.
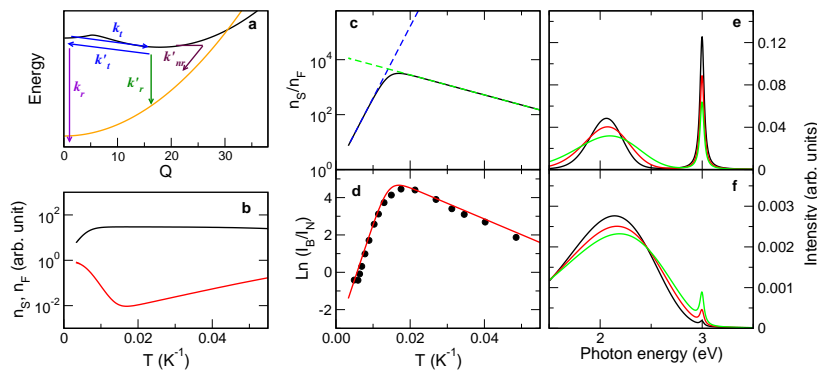
Fig. 3 Temperature dependence of exciton densities and luminescence. (a) Schematic diagram showing transition paths of FEs and STEs. (b) n_S (black line) and n_F (red line) as a function of reciprocal temperature. (c, d) plot ratio n_S/n_F and logarithm I_B/I_N as a function of reciprocal temperature. (e, f) plot luminescence spectra at low-temperature and high-temperature regimes. In (c), dashed blue and green lines plot e^{-E_S/k_BT} and $(k_t^0/k_r')e^{-E_B/k_BT}$, respectively. In (d) black dots are experimental data of (HIS)PbBr$_4$ reported in Ref.[19]. Black, red, and green lines correspond to $T = 15$, 30, and 60 K in (e) and 120, 150, and 180 K in (f).

An in-plane tilt has $\theta = 0$ and $\boldsymbol{d}_i'(\theta, \phi) = d_0 e^{i\phi} \boldsymbol{e}_+$, which remains circularly polarized, and thus does not affect dipole-dipole coupling or the bandwidths in Eq. (6). Nor does it alter the ODP strength due to both the QW thickness l_a and the relevant X-Pb-X vibration direction remaining unchanged.

By contrast, an out-of-plane tilt has $\theta \neq 0$, and $\boldsymbol{d}_i'(\theta, \phi)$, according to Eq. (13), is no longer circular polarized along $\boldsymbol{e}_+$ but a mixture of polarizations along $\boldsymbol{e}_+$, $\boldsymbol{e}_-$ and $\boldsymbol{e}_z$. With such a tilt, two adjacent PbX$_6$ octahedra within a layer have $\theta_1 = -\theta_2 = \theta$, $\phi_1 = -\phi_2 = \phi$, while those across layers have $\theta_1 = \theta_2 = \theta$, $\phi_1 = \phi_2 = \phi$, as illustrated in Fig. 4a, and as a result, the intra- and inter-layer bandwidths for small θ become

$$B_\perp \simeq \frac{2e^2\hbar^2 f_\perp}{mE_g a^3} \cos^2\theta, \; B_z = \frac{2e^2\hbar^2 f_\perp}{mE_g c^3}\left(1 - \frac{3}{2}\sin^2\theta\right). \qquad (14)$$

Thus out-of-plane tilting reduces both intra- and inter-layer bandwidths, with a more pronounced effect on the latter, as delineated in Fig. 4c.

An out-of-plane tilt also modifies the ODP strength. Such a tilt would reduce the thickness of Pb-X layers from l_a to $l_a' = l_a \cos\theta$. Moreover, a dilation or compression of X-Pb-X bond length δu contributes only partially to the variation in the Pb-X layer thickness, $\delta z = \delta u \cos\theta$, as illustrated in Fig. 4b. Consequently, the effective ODP strength becomes $\gamma/\cos^2\theta$ according to Eq. (3). Both the reduction in bandwidths and the increase of ODP strength, as discussed earlier, will enhance formation of STEs. We see in Fig. 4b that the STE energy gain $-E_S$ rapidly increases with the out-of-plane tilting angle θ, which satisfactorily explains the observed θ-dependence of $\ln(I_B/I_N)$ for several 2D HOIPs [20]. To account for the experimental data, the tilting effects on both the exciton bandwidths and the ODP strength are important, as indicated by the significant difference between the solid and dashed lines in Fig. 4d. We note that while the experimental data in Fig. 4d appear to be linearly dependent on θ, the theoretical curves are parabolic at small θ because both the ODP and exciton bandwidths are even function of θ, which are consistent with the fact that θ and $-\theta$ correspond to the same torsion.

4.2   Corrugated 2D HOIPs

While the STE model presented above was developed with flat 2D HOIPs in mind, the quintessence of the model, namely, the interplay of the exciton bandwidths and the ODP, is in fact more general and can be applied to corrugated 2D HOIPs as well. Corrugated 2D HOIPs, while less common than flat ones, possess highly desirable attributes for optoelectronic applications. In fact, the broadband white-light luminescence was first discovered in corrugated 2D HOIPs [14]. In addition, the depth n of a corrugated structure can be systematically varied, introducing another degree of freedom for tailoring 2D HOIPs [25]. A recent study shows that a corrugated $n = 3$ 2D bromide emits a much broader luminescence as compared to a flat one [25]. In such a corrugated 2D structure, as illustrated in Fig. 5, the quantum confinement and associated ODP resemble those of a flat structure. The major difference lies in the arrangement of adjacent PbX$_6$ octahedra: In the flat structure, each octahedron is surrounded by four adjacent octahedra in

the x-y plane, whereas in the corrugated one, only two adjacent octahedra (along the x-axis) are in the x-y plane and the other two having an angle of $\pi/4$ against the plane. Consequently, the dipole-dipole coupling strengths along the x- and y-axes, t_x and t_y, are different, $|t_y| = |t_x|/2$, indicating that the exciton bandwidth along the y-axis is only half of that in a flat structure. With a decrease in the exciton bandwidth under a same ODP strength, STEs would have a larger lattice distortion and greater energy gain $-E_S$, as shown in Fig. 5b, where PESs for different $B_\perp$ are plotted. Here to apply our modeling results for isotropic intralayer exciton bandwidth, $B_\perp = 8|t_x| = 8|t_y| = B_0$, to the corrugated structure, we consider two cases with $B_\perp = 8\sqrt{|t_x t_y|} = B_0/\sqrt{2}$ in one and $B_\perp = 8|t_y| = B_0/2$ in the other. The two cases set the upper and lower limits for the STE energy in the corrugated structure, as the smaller one of $|t_x|$ and $|t_y|$ controls the onset of STE formation. The computed luminescence spectra for $B_\perp = B_0/\sqrt{2}$ and $B_0/2$, as displayed in Fig. 5b, are much broader than that for the flat structure with $B_\perp = B_0$, consistent with experiment. This agreement on corrugated structures further supports the notion that STEs in 2D HOIPs are determined by the interplay of the exciton bandwidths and the ODP.

5   Conclusions

We have shown that the driving force of the STEs in 2D HOIPs is the strong ODP arising from fluctuation in Pb-X QW's thickness. Many unusual properties of STEs in 2D HOIPs observed experimentally can be unravelled by the interplay of the ODP and the exciton bandwidth. Since broadband luminescence is largely dictated by the STE's PES, to achieve a white luminescence, one can reduce the exciton bandwidth and/or enhance the ODP strength. To have a strong ODP, according to Eq. (3), it is desirable to have a small Pb-X QW thickness. Hence single layered QW structures is more preferable than thicker 2D HOIPs such as those in high-order Ruddlesden-Popper series. In addition, out-of-plane octahedral tilting can reduce the effective QW thickness and therefore enhance the ODP strength. Furthermore, a small reduced mass of exciton, μ, would make excitons more susceptible to the quantum confinement, leading to an increase in the ODP. To achieve a narrow exciton bandwidth along the z-axis, B_z, one can use a long organic ion to increase the interlayer distance. The intra-layer exciton bandwidth $B_\perp$ can be reduced by introducing out-of-plane octahedral tilting in flat structures or employing corrugated structures. The high tunability afforded by the 2D HOIPs indicate the STEs properties can be systematically tailored for broad applications in optoelectronics.

Since the ODP in 2D HOIPs originates from thickness fluctuations of Pb-X QWs, it strongly couples to not only excitons but also electrons and holes, as shown in Fig. 1b, and would contribute to carrier scattering. Moreover, a strong ODP may trap electrons and holes, resulting in small electron and hole polarons [44]. Note that the small polarons in 2D HOIPs, which originates from the unique ODP in 2D systems, are distinct from those in 3D HOIPs [29], which may arise when the polar coupling is strong. The ODP-induced carrier scattering and small polaron formation can drastically influence charge transport, particularly across layers. Transport of small polarons is usually via hopping [45], which is
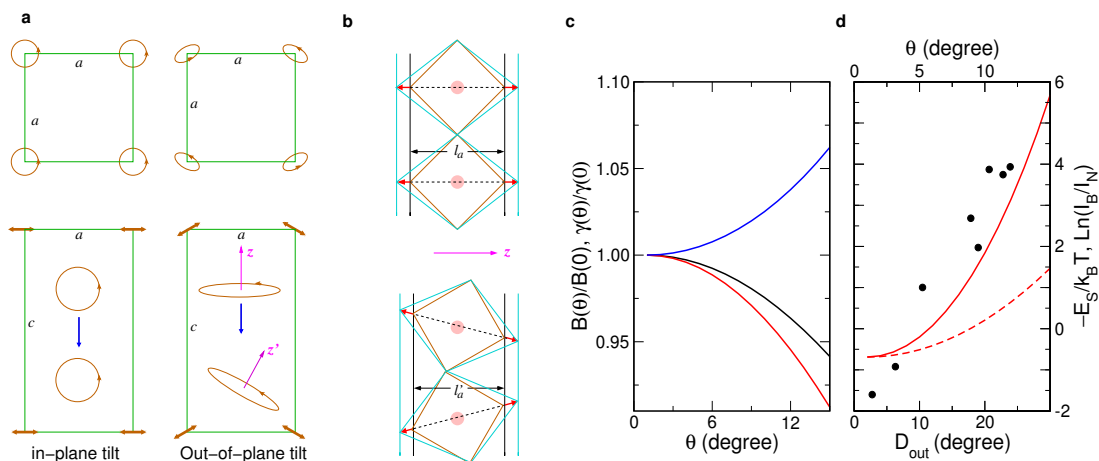
Fig. 4 PbX$_6$ tilting effects. (a, b) Schematic diagrams showing in-plane and out-of-plane tilting effects on transition dipoles and on the ODP. (c) Exciton bandwidths $B_\perp$ and B_z and ODP strength γ as a function of out-of-plane tilt θ. (d) Comparison between calculated $-E_S/k_B T$ and experimentally measured $\ln(I_B/I_N)$ (black dots) from Ref. [19] versus out-of-plane tilting. In (a), upper and lower panels illustrate the intra- and inter-layer dipole configurations. Circles (double-headed arrows) represent circularly polarized transition dipoles in the Pb-X layer from top view (side view). An in-plane tilting does not alter the circular polarization whereas an out-of-plane tilting changes both polarization direction and ellipticity. In (b), the upper (lower) panel shows the Pb-X layer thickness and vibration directions with an in-plane (out-of-plane) tilt. In (c), black, red, and blue lines correspond to $B_\perp(\theta)/B_\perp(0)$, $B_\perp(\theta)/B_\perp(0)$, and $\gamma(\theta)/\gamma(0)$, respectively. In (d), solid and dashed lines in the lower panel correspond to $\gamma = 0.0826/\cos^2\theta$ and $\gamma = 0.0826$ eV, respectively. The experimentally determined out-of-plane $D_{\text{out}} \simeq 2\theta$. Other parameters are $T = 80$ K, $B_\perp(0) = 0.42$ eV, and $B_z(0) = 0.13$ eV.
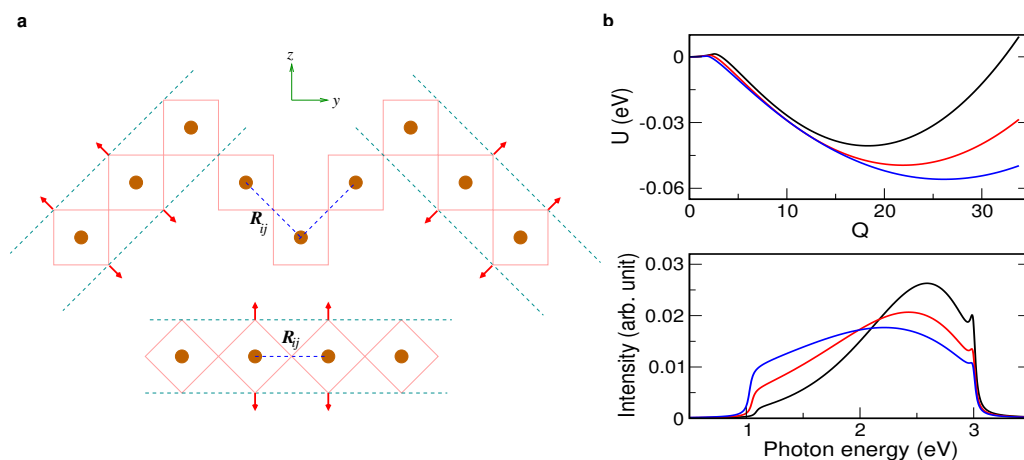
Fig. 5 Corrugated 2D HOIPs. (a) Schematic diagram showing different PbX$_6$ arrangements in corrugated and flat 2D HOIPs. (b) PESs of STEs (upper panel) and luminescence spectra (lower panel) for flat and corrugated structures at room temperature. In (a), upper and lower panels illustrate PbX$_6$ octahedra and ODP of the corrugated (011) and flat (001) 2D HOIPs in the y-z plane. Red arrows indicate the B_{1g} mode that alters the QW thickness. In (b), black, red, and blue linse correspond to $B_\perp = B_0$, $B_0/\sqrt{2}$, and $B_0/2$, respectively. Parameters are $\gamma = 0.0449$ eV and $B_0 = 0.12$ eV.

a thermal activation process and qualitatively different from band-like transport of large polarons[46] in 3D HOIPs. Hence 2D HOIPs are expected to have distinct carrier transport properties, in addition to disparate luminescence features, than 3D HOIPs, and may be exploited for novel electronic and thermoelectric applications[47].

Conflicts of interest

There are no conflicts to declare.

Acknowledgements

Notes and references

1 A. Kojima, K. Teshima, Y. Shirai and T. Miyasaka, *J. Am. Chem. Soc.*, 2009, **131**, 6050–6051.

2 L. Etgar, P. Gao, Z. Xue, Q. Peng, A. K. Chandiran, B. Liu, M. K. Nazeeruddin and M. Grätzel, *J. Am. Chem. Soc.*, 2012, **134**, 17396–17399.

3 X. Li, D. Bi, C. Yi, J.-D. Décoppet, J. Luo, S. M. Zakeeruddin, A. Hagfeldt and M. Grätzel, *Science*, 2016, **353**, 58–62.

4 M. Hirasawa, T. Ishihara and T. Goto, *J. Phys. Soc. Jpn.*, 1994, **63**, 3870–3879.

5 B. Saparov and D. B. Mitzi, *Chem. Rev.*, 2016, **116**, 4558–4596.

6 H. Tsai, W. Nie, J.-C. Blancon, C. C. Stoumpos, R. Asadpour, B. Harutyunyan, A. J. Neukirch, R. Verduzco, J. J. Crochet, S. Tretiak *et al.*, *Nature*, 2016, **536**, 312.

7 I. C. Smith, E. T. Hoke, D. Solis-Ibarra, M. D. McGehee and H. I. Karunadasa, *Angew. Chem. Int. Ed.*, 2014, **53**, 11232–11235.

8 R. L. Milot, R. J. Sutton, G. E. Eperon, A. A. Haghighirad, J. Martinez Hardigree, L. Miranda, H. J. Snaith, M. B. Johnston and L. M. Herz, *Nano Lett.*, 2016, **16**, 7001–7007.

9 O. Yaffe, A. Chernikov, Z. M. Norman, Y. Zhong, A. Velauthapillai, A. van der Zande, J. S. Owen and T. F. Heinz, *Phys. Rev. B*, 2015, **92**, 045414.

10 J.-C. Blancon, A. V. Stier, H. Tsai, W. Nie, C. Stoumpos, B. Traore, L. Pedesseau, M. Kepenekian, F. Katsutani, G. Noe *et al.*, *Nat. Commun.*, 2018, **9**, 2254.

11 M. Yuan, L. N. Quan, R. Comin, G. Walters, R. Sabatini, O. Voznyy, S. Hoogland, Y. Zhao, E. M. Beauregard, P. Kanjanaboos *et al.*, *Nat. Nanotech.*, 2016, **11**, 872.

12 X. Gong, O. Voznyy, A. Jain, W. Liu, R. Sabatini, Z. Piontkowski, G. Walters, G. Bappi, S. Nokhrin, O. Bushuyev *et al.*, *Nat. Mater.*, 2018, **17**, 550.

13 Z. Guo, X. Wu, T. Zhu, X. Zhu and L. Huang, *ACS nano*, 2016, **10**, 9992–9998.

14 E. R. Dohner, E. T. Hoke and H. I. Karunadasa, *J. Am. Chem. Soc.*, 2014, **136**, 1718–1721.

15 K.-z. Du, Q. Tu, X. Zhang, Q. Han, J. Liu, S. Zauscher and D. B. Mitzi, *Inorg. Chem.*, 2017, **56**, 9291–9302.

16 C. C. Stoumpos, D. H. Cao, D. J. Clark, J. Young, J. M. Rondinelli, J. I. Jang, J. T. Hupp and M. G. Kanatzidis, *Chem. Mater.*, 2016, **28**, 2852–2867.

17 D. Wang, B. Wen, Y.-N. Zhu, C.-J. Tong, Z.-K. Tang and L.-M. Liu, *J. Phys chem. Lett.*, 2017, **8**, 876–883.

18 Z.-G. Yu, *J. Phys. Chem. Lett.*, 2017, **9**, 1–7.

19 M. D. Smith, A. Jaffe, E. R. Dohner, A. M. Lindenberg and H. I. Karunadasa, *Chem. Sci.*, 2017, **8**, 4497–4504.

20 D. Cortecchia, J. Yin, A. Bruno, S.-Z. A. Lo, G. G. Gurzadyan, S. Mhaisalkar, J.-L. Brédas and C. Soci, *J. Mater. Chem. C*, 2017, **5**, 2771–2780.

21 L. D. Landau, *Phys. Z. Sowjet.*, 1933, **3**, 664.

22 E. I. Rashba, *Optika i Spektroskopiya*, 1957, **2**, 75–87.

23 H. Sumi and Y. Toyozawa, *J. Phys. Soc. Jpn.*, 1971, **31**, 342–358.

24 D. B. Straus and C. R. Kagan, *J. Phys. Chem. Lett.*, 2018, **9**, 1434–1447.

25 L. Mao, Y. Wu, C. C. Stoumpos, M. R. Wasielewski and M. G. Kanatzidis, *J. Am. Chem. Soc.*, 2017, **139**, 5210–5215.

26 H. Fröhlich, *Adv. Phys.*, 1954, **3**, 325–361.

27 Z.-G. Yu, *J. Phys. Chem. Lett.*, 2016, **7**, 3078–3083.

28 X.-Y. Zhu and V. Podzorov, *J. Phys. Chem. Lett.*, 2015, **6**, 4758–4761.

29 A. J. Neukirch, I. I. Abate, L. Zhou, W. Nie, H. Tsai, L. Pedesseau, J. Even, J. J. Crochet, A. D. Mohite, C. Katan and S. Tretiak, *J. Phys. Chem. Lett.*, 2018, **9**, 7130–7136.

30 Z. G. Yu, *Sci. Rep.*, 2016, **6**, 28576.

31 V. A. Dragomir, S. Neutzner, C. Quarti, D. Cortecchia, A. Petrozza, S. Roorda, D. Beljonne, R. Leonelli, A. R. S. Kandada and C. Silva, *arXiv preprint arXiv:1812.05255*, 2018.

32 M. A. Pérez-Osorio, R. L. Milot, M. R. Filip, J. B. Patel, L. M. Herz, M. B. Johnston and F. Giustino, *J. Phys. Chem. C*, 2015, **119**, 25703–25718.

33 L. D. Landau and E. M. Lifshitz, *Quantum mechanics: non-relativistic theory*, Elsevier, 2013, vol. 3.

34 R. S. Knox, *Theory of Excitons*, Academy Press, 1963.

35 R. Williams and K. Song, *J. Phys. Chem. Solids*, 1990, **51**, 679 – 716.

36 D. Zhao, J. M. Skelton, H. Hu, C. La-o vorakiat, J.-X. Zhu, R. A. Marcus, M.-E. Michel-Beyerle, Y. M. Lam, A. Walsh and E. E. M. Chia, *Appl. Phys Lett.*, 2017, **111**, 201903.

37 K. Kaasbjerg, K. S. Thygesen and K. W. Jacobsen, *Phys. Rev. B*, 2012, **85**, 115317.

38 R. Fivaz and E. Mooser, *Phys. Rev.*, 1967, **163**, 743–755.

39 J. Callaway, *Quantum Theory of the Solid State*, Academy Press, 1991.

40 T. Ishihara, J. Takahashi and T. Goto, *Phys. Rev. B*, 1990, **42**, 11099–11107.

41 H. Sumi and A. Sumi, *J. Phys. Soc. Jpn.*, 1994, **63**, 637–657.

42 Z. G. Yu, A. Saxena and A. R. Bishop, *Phys. Rev. B*, 1997, **56**, 3697–3716.

43 S. Krishnamurthy and Z.-G. Yu, *Appl. Phys. Lett.*, 2017, **110**, 021113.

44 T. Holstein, *Ann. Phys.*, 2000, **281**, 725 – 773.

45 D. Emin, *Polarons*, Cambridge University Press, 2012.

46 D. C. Langreth, *Phys. Rev.*, 1965, **137**, A760–A764.

47 P. Guo, C. C. Stoumpos, L. Mao, S. Sadasivam, J. B. Ketterson, P. Darancet, M. G. Kanatzidis and R. D. Schaller, *Nat. Commun.*, 2018, **9**, 2019.